The Astrophysical Journal, 570:314–328, 2002 May 1

THE EFFECT OF THE HALL TERM ON THE NONLINEAR EVOLUTION OF THE MAGNETOROTATIONAL INSTABILITY. I. LOCAL AXISYMMETRIC SIMULATIONS

Takayoshi Sano and James M. Stone
Department of Astronomy, University of Maryland, College Park, MD 20742-2421; sano@astro.umd.edu
Received 2001 November 10; accepted 2002 January 7

ABSTRACT

The effect of the Hall term on the evolution of the magnetorotational instability (MRI) in weakly ionized accretion disks is investigated using local axisymmetric simulations. First, we show that the Hall term has important effects on the MRI when the temperature and density in the disk is below a few thousand K and between 10^{13} and 10^{18} cm^{-3}, respectively. Such conditions can occur in the quiescent phase of dwarf nova disks, or in the inner part (inside 10–100 AU) of protoplanetary disks. When the Hall term is important, the properties of the MRI are dependent on the direction of the magnetic field with respect to the angular velocity vector $\mathbf{\Omega}$. If the disk is threaded by a uniform vertical field oriented in the same sense as $\mathbf{\Omega}$, the axisymmetric evolution of the MRI is an exponentially growing two-channel flow without saturation. When the field is oppositely directed to $\mathbf{\Omega}$, however, small scale fluctuations prevent the nonlinear growth of the channel flow and the MRI evolves into MHD turbulence. These results are anticipated from the characteristics of the linear dispersion relation. In axisymmetry on a field with zero-net flux, the evolution of the MRI is independent of the size of the Hall term relative to the inductive term. The evolution in this case is determined mostly by the effect of ohmic dissipation.

Subject headings: accretion, accretion disks — diffusion — instabilities — MHD — turbulence

1. INTRODUCTION

The structure and evolution of accretion disks are largely determined by angular momentum transport processes. One of the most promising processes is MHD turbulence driven by the magnetorotational instability (MRI) (Balbus & Hawley 1991). In ideal MHD, the growth rate of the MRI is of the order of the orbital frequency Ω, and the characteristic wavelength of the most unstable mode is $2\pi v_A/\Omega$, where v_A is the Alfvén speed. The nonlinear regime of the MRI has been well studied in ideal MHD using numerical simulations. However, in some systems, accretion disks are expected to be only partially ionized, and nonideal MHD effects, which generally suppress the growth of the MRI, must be considered. For example, the low temperatures of accretion (protoplanetary) disks around young stellar objects make thermal ionization processes ineffective, so that the abundance of charged particles is very small, and nonideal MHD effects are important (Gammie 1996; Stone et al. 2000). Another example is provided by dwarf nova systems in quiescence. The temperature of the disk in this case can be well below 10^4 K and the disk is only weakly ionized, so that nonideal MHD effects are again important (Gammie & Menou 1998).

There are three regimes in nonideal MHD associated with the relative importance of different terms in the generalized Ohm's law (see § 2); they are the ambipolar diffusion, ohmic dissipation, and Hall regimes. Which term dominates depends on the ionization fraction and density of the gas. Ambipolar diffusion is most important in regions of relatively low density and high ionization (e.g., Regős 1997). The linear properties of the MRI in the ambipolar regime have been explored by Blaes & Balbus (1994); they find unstable modes exist when the collision frequency of an ion with neutrals is higher than the orbital frequency. The nonlinear evolution of the MRI in this regime was examined by Hawley & Stone (1998) using two fluid simulations. They found that when the coupling between ions and neutrals is weak, the turbulence in the ionized component of the plasma excited by the MRI does not affect the motion of neutrals very much, thus significant angular momentum transport requires a greater coupling between the ions and neutrals than that required for linear instability. Brandenburg et al. (1995) and Mac Low et al. (1995) also studied the effect of the ambipolar diffusion in the strong coupling limit in a few models.

Ohmic dissipation becomes important when the ionization fraction of the gas is very low. In this case, a linear analysis (Jin 1996; Sano & Miyama 1999) shows that small-wavelength perturbations are damped, and the characteristic wavelength of the MRI increases in comparison to the ideal MHD case. The axisymmetric two-dimensional evolution of the MRI demonstrates that nonlinear saturation can occur due to ohmic dissipation (Sano, Inutsuka, & Miyama 1998), even though the corresponding ideal MHD cases show an ever-growing channel flow without saturation (Hawley & Balbus 1992). Fleming, Stone, & Hawley (2000) examined the nonlinear evolution using local three-dimensional simulations; they found that dissipation weakens the MHD turbulence. For significant turbulence and angular momentum transport to occur, a critical value for the magnetic Reynolds number must be exceeded, and this value depends on the field geometry in the disk.

Recently, linear analyses of the MRI in the Hall regime have been presented by Wardle (1999) and Balbus & Terquem (2001). The maximum growth rate and characteristic wavelength of the MRI are strongly modified by the Hall effect. Most interesting is that the linear properties of the instability depend on the direction of the magnetic field. This is because the dispersion relation for incompressible Alfvén waves traveling along field lines is quite different in

Hall MHD. In particular, the left- and right-circularly polarized Alfvén waves have different phase velocities, and these two waves interact with the Coriolis force in the disk in different ways. One of these two waves is commonly referred to as the whistler wave.

The purpose of this paper is to investigate the effect of the Hall term on the nonlinear evolution of the MRI in axisymmetry. When the Hall term is important, ohmic dissipation often cannot be neglected (Balbus & Terquem 2001). Thus, we solve an induction equation that includes both ohmic dissipation and the Hall effect. The plan of this paper is as follows. We examine when the Hall term becomes important in dwarf nova and protoplanetary disks in § 2. Our numerical method and the initial conditions are described in § 3. The results of two-dimensional MHD simulations are presented in § 4 for both a uniform and a zero-net flux vertical field. The application of the results to actual accretion disks is discussed in § 5, and our results are summarized in § 6.

2. THE HALL REGIME IN ACCRETION DISKS

In this section we examine when the Hall term becomes important in actual accretion disks. We consider a weakly ionized fluid composed of ions, electrons, and neutrals. Charged dust grains can be important in some situations (Wardle & Ng 1999; Sano et al. 2000), because the ionization fraction of the plasma is strongly affected by the abundance and size distribution of the grains through recombination processes on grain surface. If dust grains with the interstellar MRN size distribution (Mathis, Rumpl, & Nordsieck 1977) are considered, the Hall term is important for densities between 10^7 and 10^{11} cm^{-3} (Wardle & Ng 1999). At these densities, negatively charged grains and positively charged ions are the dominant charge carriers. At higher densities than 10^{11} cm^{-3}, both the negative and positive charge carriers are grains, and the dynamics is dominated by ohmic dissipation. The expected density of protoplanetary disks is higher than the Hall regime in a dusty plasma; thus, if dust is present most of the disk will be in the ohmic dissipation regime (Wardle & Ng 1999). However, this assumes the dust grains are well mixed and are unevolved. In fact, dust grains in the disk may grow in size through collisions and/or sediment toward the midplane. These evolutionary effects reduce the abundance of charged grains, so that ions and electrons become the dominant charge carriers even in very dense regions (Sano et al. 2000). On the other hand, whether the gas flow in the disk is laminar or turbulent can largely affect the evolution of the grains (e.g., Cuzzi, Dobrovolskis, & Champney 1993; Hodgson & Brandenburg 1998). Self-consistent models of dusty disks which include the effects of gravitational settling, turbulent mixing, and grain growth are beyond the scope of this paper. The analysis presented here, which does not include the effect of dust grains, could be applicable to protoplanetary disks in the late stages of evolution. Dust is not expected to be important in dwarf nova disks.

Charge neutrality, $n_e = n_i$, is assumed, where n_e and n_i are the number densities of electrons and ions, respectively. The coupling between charged particles and neutrals depends on the collision rate $\langle \sigma v \rangle_\alpha$, where α is i (ions) and e (electrons). Here, we adopt the values $\langle \sigma v \rangle_i = 1.9 \times 10^{-9}$ cm^3 s^{-1} and $\langle \sigma v \rangle_e = 8.28 \times 10^{-10} T^{1/2}$ cm^3 s^{-1} (Draine, Roberge, & Dalgarno 1983). The imperfect coupling between electrons and neutrals results in a finite electrical conductivity,

$$\sigma_c = \frac{e^2 n_e}{m_e \nu_e}, \tag{1}$$

where e and m_e are the electron charge and mass. The electron-neutral collision frequency is $\nu_e = n_n \langle \sigma v \rangle_e$, where n_n is the number density of neutrals. The associated magnetic diffusivity is

$$\eta = \frac{c^2}{4\pi\sigma_c}, \tag{2}$$

where c is the speed of light. The cyclotron frequencies of the ions and electrons are

$$\omega_{c\alpha} = \frac{eB}{m_\alpha c}, \tag{3}$$

where α is i and e.

The induction equation including the terms of the ohmic dissipation, the Hall effect, and the ambipolar diffusion is given by

$$\frac{\partial \boldsymbol{B}}{\partial t} = \boldsymbol{\nabla} \times \left[\boldsymbol{v} \times \boldsymbol{B} - \frac{4\pi\eta \boldsymbol{J}}{c} - \frac{\boldsymbol{J} \times \boldsymbol{B}}{e n_e} + \frac{(\boldsymbol{J} \times \boldsymbol{B}) \times \boldsymbol{B}}{c\gamma\rho_i\rho} \right], \tag{4}$$

where $\boldsymbol{v}$ is the neutral velocity and

$$\boldsymbol{J} = \frac{c}{4\pi} (\boldsymbol{\nabla} \times \boldsymbol{B}) \tag{5}$$

is the current density. The drag coefficient is

$$\gamma = \frac{\langle \sigma v \rangle_i}{m_i + m_n}, \tag{6}$$

where m_i and $m_n = \mu m_{\rm H}$ are the ion and neutral particle mass, μ is the mean molecular weight of the gas, and $m_{\rm H}$ is the mass of a hydrogen atom.

Here we estimate the relative magnitude of the four terms on the right-hand side of the induction equation. Following Balbus & Terquem (2001), we denote these terms (reading from left to right) as I (inductive), O (ohmic), H (Hall), and A (ambipolar). The ratios A/H and H/O are given by

$$\frac{A}{H} = \frac{\omega_{ci}}{\gamma\rho}, \tag{7}$$

and

$$\frac{H}{O} = \frac{\omega_{ce}}{\nu_e}. \tag{8}$$

Note that these ratios are determined only by microphysical quantities. In this paper we define the Hall regime as the conditions under which the Hall term is the largest of the three nonideal MHD effects. From equations (7) and (8), in the Hall regime electrons are coupled to the magnetic field ($\omega_{ce}/\nu_e > 1$), but ions are not ($\omega_{ci}/\gamma\rho < 1$) because of the collisions with neutrals. In low-density regions, both ions and electrons are coupled to the magnetic field: this is the ambipolar diffusion regime ($A > H > O$). On the other hand, in the high-density regions, both the electrons and ions are decoupled from the field, leading to the ohmic dissipation regime ($O > H > A$). The density range of the Hall regime is therefore intermediate between these two (see below).

The importance of each nonideal MHD effect relative to the inductive term is

$$\frac{O}{I} = \frac{\eta}{VL} = \frac{\eta\Omega}{v_{\rm A}^2} \equiv Re_M^{-1} , \tag{9}$$

$$\frac{H}{I} = \frac{cB}{4\pi e n_e VL} = \frac{cB\Omega}{4\pi e n_e v_{\rm A}^2} \equiv \frac{X}{2} , \tag{10}$$

and

$$\frac{A}{I} = \frac{B^2}{4\pi\gamma\rho_i\rho VL} = \frac{\Omega}{\gamma\rho_i} \tag{11}$$

for the ohmic dissipation, the Hall effect, and the ambipolar diffusion, respectively, where V and L are typical values for the velocity and length scale in the fluid. We assume that V is of the order of $v_{\rm A}$ and that $L = v_{\rm A}/\Omega$, i.e., the characteristic scale of the MRI. Equations (9) and (10) give the definition of two important nondimensional parameters; the magnetic Reynolds number Re_M and the Hall parameter X. The relation between these two parameters is given by

$$\frac{H}{O} = \frac{\omega_{ce}}{\nu_e} = \frac{X\mathrm{Re}_M}{2} . \tag{12}$$

This is independent of the ionization fraction and the choice of the typical scales V and L, and constrains the values of X and Re_M in the Hall regime. Note that the definition of the Hall parameter X is the same as x in Balbus & Terquem (2001) (in this paper we shall use x to denote one of the coordinates in our computational domain). The importance of the Hall effect is estimated by the ratio H/I, or X. In order to evaluate this ratio in actual disks, we need to know the number density of electrons n_e. In the following subsections, we calculate the ionization fraction, n_e/n_n, in dwarf nova and protoplanetary disks.

2.1. *Dwarf Nova Disks in Quiescence*

In outburst, the typical temperature of dwarf nova disks is over 10^4 K so that the gas is fully ionized (e.g., Cannizzo 1993). However, in quiescence the temperature is only a few thousand K. The main source of free electrons at this temperature is thermal ionization of Na, Al, and K. Assuming the mean mass of ions is $m_i = 30 m_{\rm H}$, and the neutrals are hydrogen atoms ($\mu = 1.27$), equations (7)–(9) give

$$\frac{A}{H} = \left(\frac{3.0\times10^{13}}{n_n}\right)^{1/2}\left(\frac{T}{10^3\ \mathrm{K}}\right)^{1/2}\left(\frac{c_s}{v_{\rm A}}\right)^{-1} , \tag{13}$$

$$\frac{H}{O} = \left(\frac{7.8\times10^{17}}{n_n}\right)^{1/2}\left(\frac{c_s}{v_{\rm A}}\right)^{-1} , \tag{14}$$

and

$$\frac{O}{I} = 1.1\times10^{-9}\left(\frac{n_e}{n_n}\right)^{-1}\left(\frac{T}{10^3\ \mathrm{K}}\right)^{-1/2} \times\left(\frac{c_s}{v_{\rm A}}\right)^{2}\left(\frac{M}{M_\odot}\right)^{1/2}\left(\frac{r}{10^{10}\ \mathrm{cm}}\right)^{-3/2} , \tag{15}$$

where r is the distance from the central star, which has mass M. For $M = M_\odot$, $T = 10^3$ K, and $v_{\rm A}/c_{\rm s} = 1$, the density range of the Hall regime is $10^{13} \lesssim n_n \lesssim 10^{18}$ cm^{-3}. The typical density of a dwarf nova disk in quiescence is $n_n \sim 10^{18}$ cm^{-3} (Gammie & Menou 1998), so that the disk is in the Hall regime. The ratio H/O varies from unity to $160(T/10^3\ \mathrm{K})^{-1/2}$ in the Hall regime, so that

$$2 \lesssim |X|\mathrm{Re}_M \lesssim 320\left(\frac{T}{10^3\ \mathrm{K}}\right)^{-1/2} . \tag{16}$$

The ratios of nonideal MHD terms to the inductive term in the induction equation (4) are functions of the ionization fraction n_e/n_n. The electron density n_e in dwarf nova disks comes from solving the Saha equation for Na, Al, and K assuming solar abundances. Figure 1 shows the ratios H/I, O/I, and A/I as a function of the number density of neutrals n_n. We assume $c_s/v_{\rm A} = 1$ and $r = 10^{10}$ cm in this figure. When the ratio H/I takes a value greater than unity, the Hall effect changes the linear character of the MRI (Balbus

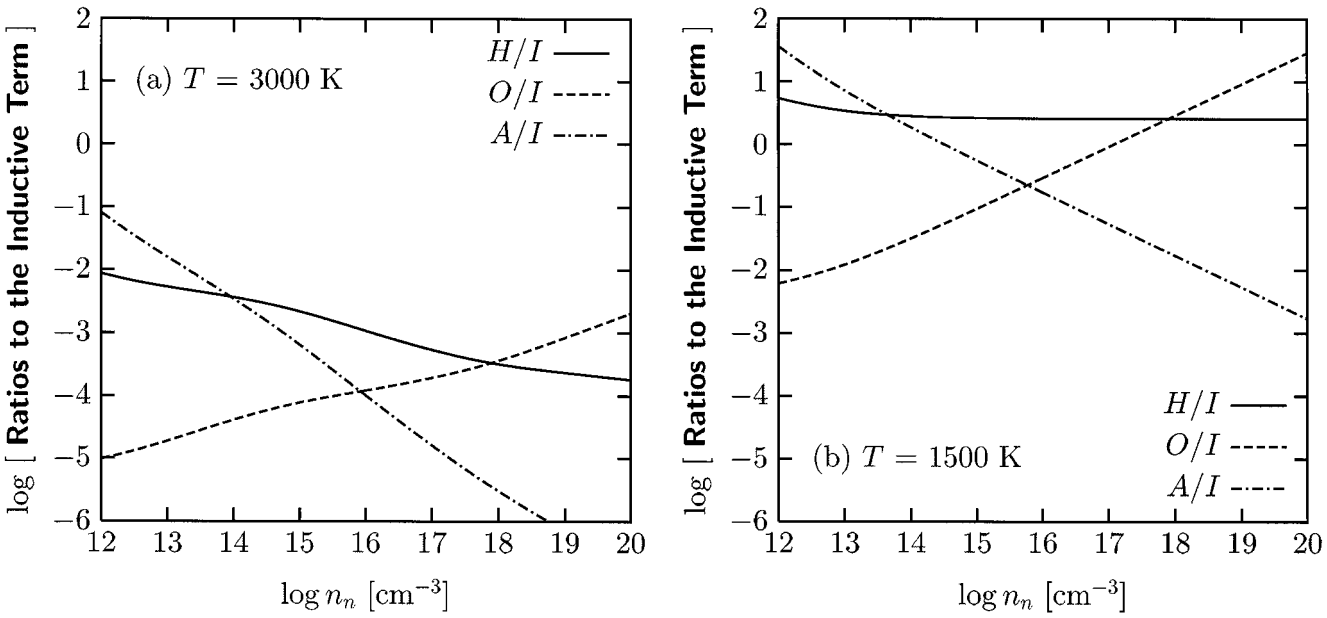

FIG. 1.—Ratios of nonideal MHD terms to the inductive term given by eqs. (9)–(11) for the case of a dwarf nova disk in quiescence for (*a*) $T = 3000$ K and (*b*) $T = 1500$ K.

& Terquem 2001). This ratio is found to be very sensitive to the temperature of the disk.

For $T = 3000$ K, the typical value of $|X|$ in the Hall regime is 10^{-3} at $n_n \sim 10^{18}$ cm^{-3}, so that the Hall term is dominant, but not large enough to affect the linear growth of the MRI. The magnetic Reynolds number $\mathrm{Re}_M = (O/I)^{-1} \sim 10^4$ in this case, implying that ohmic dissipation is also unimportant at this temperature. When $\mathrm{Re}_M \lesssim 1$, ohmic dissipation reduces the linear growth rate of the MRI (Sano & Miyama 1999) and the amplitude of the Maxwell stress at saturation (Sano & Inutsuka 2001). Note that we use a different definition of Re_M than Fleming et al. (2000), which changes this critical value (see § 5.2). The ratios shown in Figure 1 depend on the field strength, or c_s/v_A (see eqs. [13]–[15]). The Hall parameter increases when c_s/v_A increases because $H/I = |X|/2 \propto c_s/v_\mathrm{A}$. For the case with $c_s/v_\mathrm{A} = 1000$, the Hall parameter is order unity, with a corresponding shift in the density range of the Hall regime to $10^{10} \lesssim n_n \lesssim 10^{15}$ cm^{-3}.

For $T = 1500$ K, the Hall parameter $|X| \sim 1$, and the Hall term can play an important role in the evolution of the MRI. The magnetic Reynolds number $\mathrm{Re}_M = (O/I)^{-1} \sim$ 1–100 at this temperature. Therefore, both the Hall effect and ohmic dissipation are essential to the evolution of the MRI in dwarf nova disks when the temperature is less than 1500 K.

2.2. *Protoplanetary Disks*

The temperatures of protoplanetary disks are very low, so that the only sources of ionization are nonthermal, e.g., cosmic rays (Umebayashi & Nakano 1988; Gammie 1996), X-rays (Igea & Glassgold 1999), and the decay of radioactive elements. We shall briefly investigate which nonideal MHD effects are important at different radii in the midplane of several disk models.

We assume a power-law distribution for the column density Σ and the temperature T,

$$\Sigma(r) = \Sigma_0 \left(\frac{r}{1\ \mathrm{AU}} \right)^{-p_1} \tag{17}$$

and

$$T(r) = T_0 \left(\frac{r}{1\ \mathrm{AU}} \right)^{-p_2}, \tag{18}$$

where the mass of the central star is set to be $M = M_\odot$. The minimum-mass solar nebula is chosen as a fiducial model; $\Sigma_0 = 1.7 \times 10^3$ g cm^{-2}, $p_1 = 3/2$, $T_0 = 280$ K, and $p_2 = 1/2$. The sound speed is $c_s(r) = [kT(r)/\mu m_\mathrm{H}]^{1/2}$, where k is the Boltzmann constant and $\mu = 2.34$ is the mean molecular weight. The angular velocity is $\Omega(r) = (GM_\odot/r^3)^{1/2}$, where G is the gravitational constant. For simplicity, cosmic rays and radioactive elements are considered as the only sources of ionization. The ionization rate due to cosmic rays, ζ_CR, is dominant because ζ_CR is about 5 orders of magnitude larger than the ionization rate due to radioactive elements ζ_R. But cosmic rays cannot penetrate into the disk more than the attenuation length $\chi_\mathrm{CR} \approx 96$ g cm^{-2} (Umebayashi & Nakano 1981). Thus, the ionization rate at the midplane decreases dramatically if the column density of the disk exceeds χ_CR. The ionization rate at the midplane is given by

$$\zeta(r) \approx \zeta_\mathrm{CR} \exp\left[-\frac{\Sigma(r)}{2\chi_\mathrm{CR}} \right] + \zeta_\mathrm{R}\ , \tag{19}$$

where $\zeta_\mathrm{CR} \approx 10^{-17}$ s^{-1} and $\zeta_\mathrm{R} \approx 6.9 \times 10^{-23}$ s^{-1}.

The ionization fraction at the ionization-recombination equilibrium is approximately given by

$$\frac{n_e}{n_n} = \sqrt{\frac{\zeta}{\beta n_n}}, \tag{20}$$

where $\beta = 1.1 \times 10^{-7} (T/300\ \mathrm{K})^{-1}$ is the dissociative recombination rate (Millar, Farquhar, & Willacy 1997). The number density of electrons n_e is a function of n_n at the midplane, which is

$$n_n(r) = \frac{\Sigma(r)}{\sqrt{\pi}\mu m_\mathrm{H} H(r)}\ , \tag{21}$$

where $H(r) = c_s(r)/\Omega(r)$ is the scale height of the disk. For the magnetic field strength we simply assume $c_s/v_\mathrm{A} = 1$ or 10 at the midplane.

Figure 2 shows the radial distribution of the ratios H/I, O/I, and A/I at the midplane for the fiducial model with (*a*) $c_s/v_\mathrm{A} = 1$ and (*b*) $c_s/v_\mathrm{A} = 10$. When $c_s/v_\mathrm{A} = 1$, the dominant term is the Hall effect within 10 AU, while ambipolar diffusion dominates in the outer parts of the disk. When the collision frequency $\gamma\rho_i/\Omega = (A/I)^{-1}$ is greater than unity, the disk is linearly unstable for axisymmetric perturbations (Blaes & Balbus 1994). Thus, the outer region of the disk is marginally unstable to the MRI.

From equation (14) the ratio H/O is always larger than unity when the density of neutrals is $n_n \lesssim 10^{18} (c_s/v_\mathrm{A})^{-2}$ cm^{-3}. Note that this is independent of the ionization fraction. Thus, the Hall effect is more important than ohmic dissipation almost everywhere in protoplanetary disks. The ratio H/O becomes larger as the density decreases, or the distance from the star r increases. The outer part of the disk has a higher ionization fraction because of its lower density. This means that both H and O decrease as r increases. We define r_O and r_H as the radii where the ratios O/I and H/I equal unity. The Hall term is important within $r < r_H$.

Protoplanetary disks can therefore be divided into three regions: (1) $r > r_H$, (2) $r_O < r < r_H$, and (3) $r < r_O$. In the outer part of the disk ($r > r_H$), both the Hall effect and ohmic dissipation are unimportant ($|X| < 1$ and $\mathrm{Re}_M \gg 1$). The critical radius r_H is about 10 AU in the fiducial model with $c_s/v_\mathrm{A} = 1$. At intermediate radii ($r_O < r < r_H$), the Hall term becomes important ($|X| > 1$) but ohmic dissipation still can be ignored ($\mathrm{Re}_M > 1$). For the region within r_O, the ionization fraction is so low that both effects are important ($|X| \gg 1$ and $\mathrm{Re}_M \ll 1$). In the fiducial model the critical radius $r_O \sim 1$ AU. In the innermost part of the disk $r \lesssim 0.1$ AU, thermal ionization is efficient, and the gas becomes well coupled to the magnetic field.

The critical radius r_H is very sensitive to the field strength. For example, almost all of the disk within 100 AU is in the Hall regime for the case $c_s/v_\mathrm{A} = 10$, as shown by Figure 2*b*. The Hall parameter increases from 1 to 10^5 as the radius r decreases from 100 to 1 AU. The change in the critical radius r_O is small. Within $r = r_O$ the magnetic Reynolds number is very small (1–10^{-4}). The ratio A/I is independent of c_s/v_A.

The dependence of r_H and r_O on the distribution of the column density is summarized in Table 1. Disk models with $p_1 = 3/2$ and 1 are examined for two different disk masses M_disk. The dependence of the critical radii on p_1 is very weak in these cases. As the disk mass is increased, the density at the midplane increases, so that the ionization fraction

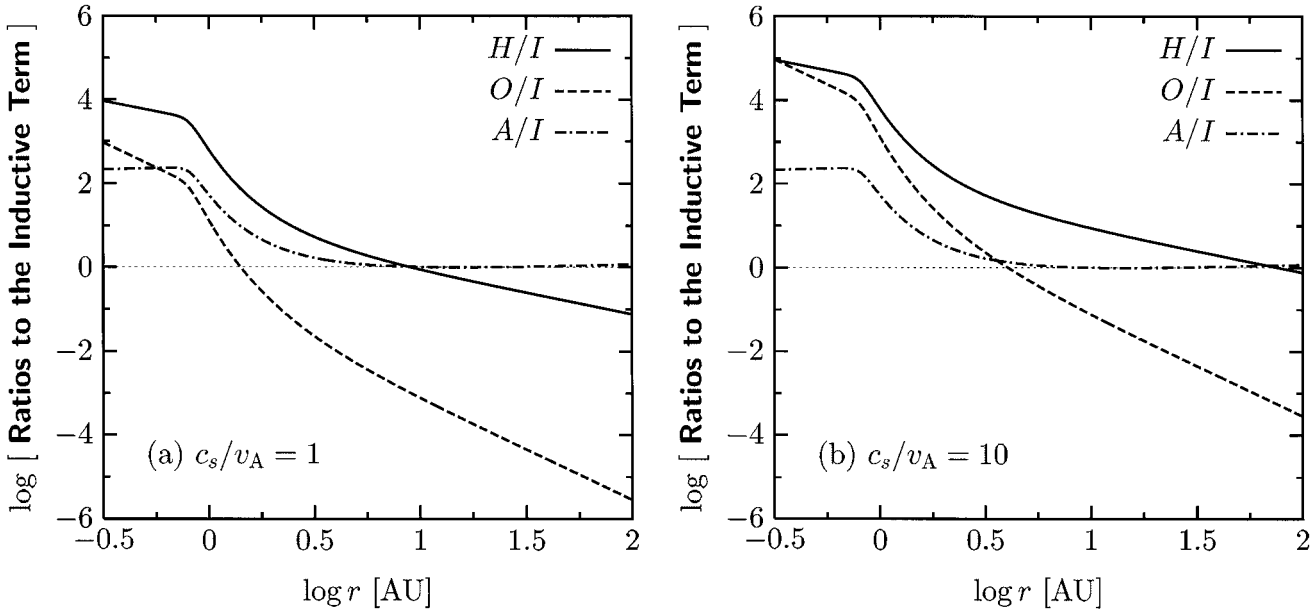

FIG. 2.—Ratios of nonideal MHD terms to the inductive term given by eqs. (9)–(11) for the case of a protoplanetary disk with (*a*) $c_s/v_A = 1$ and (*b*) $c_s/v_A = 10$.

decreases and the critical radii shift outward in both cases. The density at the midplane also increases when the temperature decreases, because the scale height of the disk H is proportional to $T^{1/2}$ (see eq. [21]). Furthermore, the recombination rate increases as the temperature decreases. Thus, a lower temperature means a lower ionization fraction. If a constant temperature $T = 10$ K is assumed everywhere in the disk, the critical radii become $r_O = 2.9$ AU and $r_H = 36$ AU for the fiducial Σ distribution with $c_s/v_A = 1$.

In all of the models examined here, a large part of the disk ($r < r_H \sim 10$–100 AU) is in the Hall regime, while the inner regions ($r < r_O \sim 1$–5 AU) are very resistive ($\mathrm{Re}_M < 1$). As discussed at the start of this section, this picture could be modified by the effect of dust grains (Wardle & Ng 1999; Sano et al. 2000).

3. NUMERICAL METHOD

3.1. *Equations and Algorithms*

We solve the equations of nonideal MHD in a local Cartesian frame of reference corotating with the disk at the angular frequency Ω corresponding to a fiducial radius r_0.

TABLE 1
CRITICAL RADII IN MODELS OF PROTOPLANETARY DISK[a]

			$c_s/v_A = 1$		$c_s/v_A = 10$	
Σ_0	p_1	$M_{\rm disk}$ ($M_\odot$)[b]	r_O (AU)	r_H (AU)	r_O (AU)	r_H (AU)
1.7×10^3	3/2	0.024	1.4	8.9	4.0	76
1.7×10^4	3/2	0.24	4.7	16	9.7	80
3.3×10^2	1	0.024	0.58	8.4	2.9	76
3.3×10^3	1	0.24	2.5	14	7.4	84

[a] The temperature distribution is assumed to be $T_0 = 280$ K and $p_2 = 1/2$ for all models.
[b] The disk mass $M_{\rm disk}$ is integrated from 0.1 to 100 AU.

The coordinates in this frame, written in terms of cylindrical coordinates (r, ϕ, z), are $x = r - r_0$, $y = r_0(\phi - \Omega t)$, and z. The vertical component of gravity is ignored in this paper. For a small region Δr surrounding the fiducial radius r_0, with $\Delta r \ll r_0$, the basic equations are given by

$$\frac{\partial \rho}{\partial t} + \boldsymbol{v} \cdot \nabla \rho = -\rho \nabla \cdot \boldsymbol{v} , \tag{22}$$

$$\frac{\partial \boldsymbol{v}}{\partial t} + \boldsymbol{v} \cdot \nabla \boldsymbol{v} = -\frac{\nabla P}{\rho} + \frac{\boldsymbol{J} \times \boldsymbol{B}}{c\rho} - 2\boldsymbol{\Omega} \times \boldsymbol{v} + 2q\Omega^2 x \hat{\boldsymbol{x}} , \tag{23}$$

$$\frac{\partial \epsilon}{\partial t} + \boldsymbol{v} \cdot \nabla \epsilon = -\frac{P \nabla \cdot \boldsymbol{v}}{\rho} + \frac{4\pi\eta \boldsymbol{J}^2}{c^2 \rho} , \tag{24}$$

$$\frac{\partial \boldsymbol{B}}{\partial t} = \nabla \times \left(\boldsymbol{v} \times \boldsymbol{B} - \frac{4\pi\eta \boldsymbol{J}}{c} - \frac{\boldsymbol{J} \times \boldsymbol{B}}{e n_e} \right) \equiv \nabla \times \boldsymbol{\mathscr{E}} , \tag{25}$$

where ϵ is the specific internal energy and $\boldsymbol{\mathscr{E}}$ is the electromotive force (EMF). The term $2q\Omega^2 x$ in the equation of motion (eq. [23]) is the tidal expansion of the effective potential with a constant $q = 3/2$ for a Keplerian disk. The gas is assumed to be the ideal, with pressure $P = (\gamma - 1)\rho\epsilon$ and $\gamma = 5/3$. The induction equation (25) includes terms for both ohmic dissipation and the Hall effect.

These equations are solved using a finite-difference code (Sano, Inutsuka, & Miyama 1999) in the local shearing box developed by Hawley, Gammie, & Balbus (1995). The hydrodynamics module of our scheme is based on a second-order Godunov scheme (van Leer 1979) using a nonlinear Riemann solver that is modified to account for the effect of tangential magnetic fields. The evolution of the magnetic field is calculated with the constrained transport (CT) method (Evans & Hawley 1988), which guarantees the divergence free condition of the field, $\nabla \cdot \boldsymbol{B} = 0$, is maintained. To extend the method to include nonideal MHD effects, we use an operator split solution procedure. The MoC-CT technique (Stone & Norman 1992) is used to update the inductive term $\boldsymbol{v} \times \boldsymbol{B}$ in the EMF. The algorithm

to update the Hall EMF, $\mathscr{E}_H = -\boldsymbol{J}\times\boldsymbol{B}/en_e$, is described in detail in the Appendix.

3.2. *Initial Conditions*

Our simulations begin with Keplerian shear flow, so that in the corotating frame the azimuthal velocity is given by $v_{y0} = -q\Omega x$. Two initial field configuration are considered in this paper: a uniform vertical field $B_z = B_0$, and a zero-net flux vertical field $B_z(x) = B_0 \sin(2\pi x/L_x)$, where L_x is the box size in the radial direction. Except for the shear velocity, the initial state is uniform: $\rho = \rho_0$ and $P = P_0$.

The calculations are performed in a two-dimensional region in the radial-vertical (x-z) plane, in a volume bounded by $x = \pm H/2$ and $z = \pm H/2$, where $H \equiv (2/\gamma)^{1/2} c_{s0}/\Omega$ is the scale height of the disk. Most of the runs use a standard grid resolution of 128×128 with uniform zoning. In the vertical direction, periodic boundary condition is used. For the radial boundary, a sheared periodic boundary condition (Hawley & Balbus 1992) is adopted. We choose normalizations with $\rho_0 = 1$, $H = 1$, and $\Omega = 10^{-3}$. Then the sound velocity and gas pressure are initially $2c_{s0}^2/\gamma = 10^{-6}$ and $P_0 = 5 \times 10^{-7}$, respectively. Initial perturbations are introduced as spatially uncorrelated pressure and velocity fluctuations. These fluctuations have a zero mean value with a maximum amplitude of $|\delta P|/P_0 = 10^{-2}$ and $|\delta \boldsymbol{v}|/c_{s0} = 10^{-2}$.

This system is characterized by three nondimensional parameters, β_0, Re_{M0}, and X_0. The initial plasma beta $\beta_0 = (2/\gamma)c_{s0}^2/v_{A0}^2$ measures the initial field strength, where $v_{A0} = B_0/(4\pi\rho_0)^{1/2}$. The magnetic Reynolds number $\mathrm{Re}_{M0} = v_{A0}^2/\eta\Omega$ sets the value of the magnetic diffusivity η, which is assumed to be spatially and temporally constant in the calculation. The initial Hall parameter,

$$X_0 = \frac{cB_0\Omega}{2\pi e n_{e0} v_{A0}^2}\,, \tag{26}$$

indicates the importance of the Hall effect and determines the initial number density of electrons n_{e0}. We assume the electron abundance is constant throughout the calculation and thus $n_e = n_{e0}\rho/\rho_0$. Our simulations show that the density fluctuations in the nonlinear regime are not large, so that even if n_e is assumed to be constant (i.e., $n_e = n_{e0}$ throughout the simulation) there is little difference to the results presented here.

3.3. *Linear Growth Rate of the Magnetorotational Instability*

To test the accuracy of our numerical algorithms, as well as to summarize the effect of the Hall term on the linear dispersion relation of the MRI, we first compare numerically measured growth rates with the predictions of linear theory. Balbus & Terquem (2001) derive the dispersion relation for axisymmetric perturbations $\delta \propto \exp(ikz + \sigma t)$ on a uniform vertical field B. Using the two nondimensional parameters Re_M and X defined by equations (9) and (10), the dispersion equation can be written as

$$\tilde{\sigma}^4 + \frac{2\tilde{k}^2}{\mathrm{Re}_M}\tilde{\sigma}^3 + \mathscr{C}_2\tilde{\sigma}^2 + \frac{2\tilde{k}^2}{\mathrm{Re}_M}\left(\tilde{\kappa}^2 + \tilde{k}^2\right)\tilde{\sigma} + \mathscr{C}_0 = 0\,, \tag{27}$$

$$\mathscr{C}_2 = \tilde{\kappa}^2 + 2\tilde{k}^2 + \frac{\tilde{k}^4}{\mathrm{Re}_M^2} + \frac{\tilde{k}^2}{4}X\left(\tilde{\kappa}^2 - 4 + \tilde{k}^2 X\right), \tag{28}$$

$$\mathscr{C}_0 = \tilde{k}^2\left(1 + \frac{\tilde{\kappa}^2}{4}X\right)\left[\tilde{\kappa}^2 - 4 + \tilde{k}^2(1+X)\right] + \frac{\tilde{\kappa}^2\tilde{k}^4}{\mathrm{Re}_M^2}\,, \tag{29}$$

where $\tilde{\sigma} = \sigma/\Omega$, $\tilde{k} = kv_A/\Omega$, and $\tilde{\kappa} = \kappa/\Omega$ is the epicyclic frequency. A positive real root σ implies an unstable exponential growth of the mode.

Figure 3*a* shows the dispersion relations for $\mathrm{Re}_M = 100$ and $X = 4$, 0, -2, and -4. Since $\mathrm{Re}_M \gg 1$, the effect on growth rates of the MRI is dominated by the Hall term. The sign of the Hall parameter X is determined by the direction

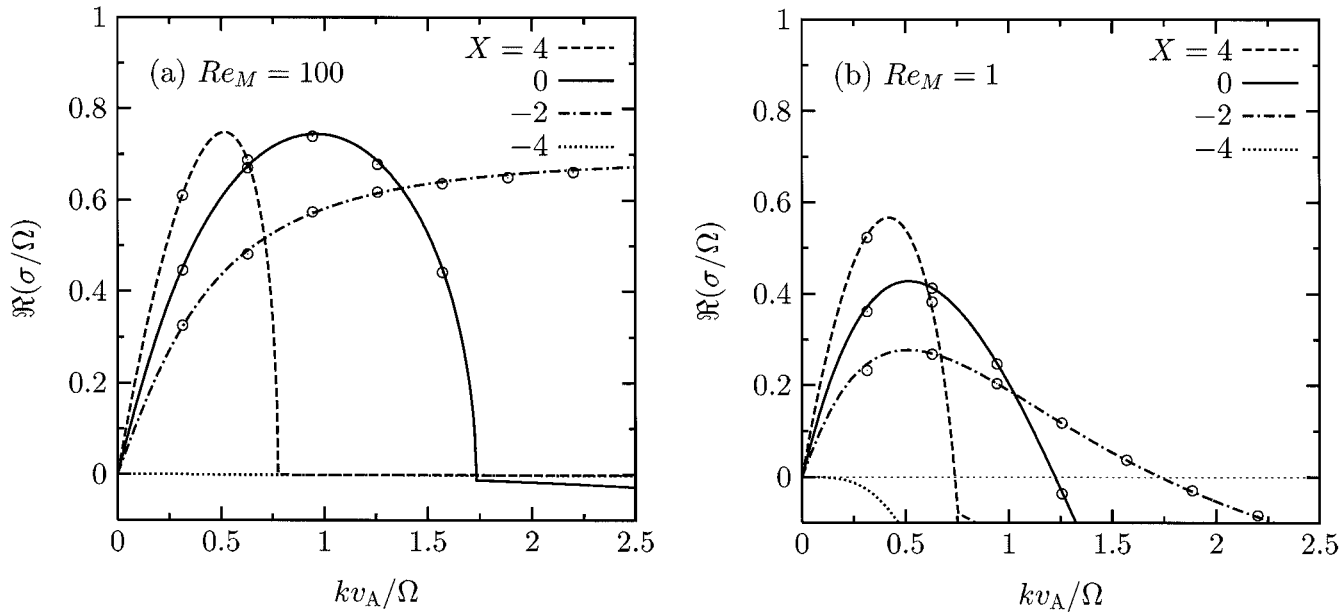

FIG. 3.—Dispersion relation for axisymmetric MRI modes for the case with (*a*) $\mathrm{Re}_M = 100$ and (*b*) $\mathrm{Re}_M = 1$. Open circles depict the numerical growth rates measured in two-dimensional numerical simulations.

of the magnetic field relative to $\mathbf{\Omega}$. Positive (negative) X denotes that the field direction is in the same (opposite) sense of $\mathbf{\Omega}$. Modes with a smaller wavenumber than the critical value $k_{\rm crit}$ are unstable for the MRI. When X is positive the critical wavenumber decreases as the Hall parameter increases. The maximum growth rate is independent of X and has the value $\tilde{\sigma}_{\rm max} \approx 0.75$, the same as the ideal MHD case. For $X < 0$, the critical wavenumber $\tilde{k}_{\rm crit} \to \infty$; the MRI has no characteristic scale in this case. On the other hand, for $X \leq -4$, no mode is linearly unstable to the axisymmetric MRI.

The dispersion relations for ${\rm Re}_M = 1$ and $X = 4$, 0, -2, and -4 are shown in Figure 3*b*. Now the maximum growth rates are significantly reduced by ohmic dissipation. Fields oriented such that X is positive produce a larger growth rate than those with negative X. The critical wavenumber for negative X remains finite in this case, and $X \leq -4$ is always linearly stable for all axisymmetric modes. Thus, the larger Hall parameter $|X|$ enhances the growth rate of the MRI in some case ($X \gg 1$ at least at small k) and completely suppresses any growth in other case ($X < -4$), depending on the field geometry.

Decreasing ${\rm Re}_M$ further leads to even smaller growth rates and critical wavenumbers. For example, at ${\rm Re}_M = 0.1$ the maximum growth rate is $\tilde{\sigma}_{\rm max} = 0.11$ (0.037) for the case of $X = 2$ (-2), while the critical wavenumber is $\tilde{k}_{\rm crit} = 0.21$ (0.12). These values are about an order of magnitude smaller than the ideal MHD case.

We have measured the growth rate of the MRI using numerical simulations with uniform B_z, $\beta_0 = 400$, and 256×256 grid zones. The simulations begin with very small random perturbations, $|\delta P|/P_0 = 10^{-6}$ and $|\delta \boldsymbol{v}|/c_{s0} = 10^{-6}$, so that any growing modes should be well described by the linear analysis during the first a few orbits of evolution. A two-dimensional Fourier decomposition of the radial velocity v_x is carried out at frequent time intervals, and the growth rates are measured for modes with zero radial wavenumber, $k_x = 0$, between orbits 2 and 2.5. These numerical growth rates are shown in Figure 3 by open circles. The numerical growth rates reproduce the analytical dispersion relation extremely well, each point is within a few percent of the predicted linear value. This provides a powerful validation of the numerical method.

4. NONLINEAR EVOLUTION OF THE MAGNETOROTATIONAL INSTABILITY

4.1. *Two-dimensional Simulations with Uniform Vertical Fields*

In the ideal MHD case, the two-dimensional MRI on a uniform B_z evolves into an exponentially growing channel flow whose amplitude is unbounded (Hawley & Balbus 1992), although saturation at finite amplitude can occur when ohmic dissipation is included (Sano et al. 1998). We now examine how these results are changed by inclusion of the Hall effect.

The initial field geometry for all models in this subsection is a uniform vertical field $B_z = B_0$, where B_0 is constant. Various models with different ${\rm Re}_{M0}$ and X_0 have been calculated and are listed in Table 2. The critical wavelength $\lambda_{\rm crit} \equiv 2\pi/k_{\rm crit}$ and the maximum growth rate $\sigma_{\rm max}$ are obtained from the dispersion equation (27). Hereafter $\langle f \rangle$ denotes the volume-averaged value of f, while $\langle\langle f \rangle\rangle$ denotes the time- and volume-averaged value. The time averaging is taken over the last 20 orbits of the calculation.

When the Hall parameter X_0 is positive, the nonlinear evolution of the MRI is quite similar to the case $X_0 = 0$. For all the models with ${\rm Re}_{M0} \gtrsim 1$ and $X_0 \geq 1$, the nonlinear evolution of the MRI goes into the two-channel flow as in the ideal MHD cases. Figure 4 shows the time evolution of the magnetic field lines in the ${\rm Re}_{M0} = 10$ and $X_0 = 2$ run (model Z5). The gray color contours denote the radial velocity v_x normalized by the initial sound speed c_{s0}. In this figure, time is given in orbits $t_{\rm rot} = 2\pi/\Omega$. In the linear phase (until about 2 orbits), the modes with the most unstable wavelength $\lambda_{\rm MRI} \sim 2\pi v_{\rm A}/\Omega$ dominate. However, because many other unstable modes are also growing, in the nonlinear regime they strongly interact leading to a transient phase of MHD turbulence.

In the turbulent phase, the vertical component of the field is amplified, and the characteristic length of the MRI in the vertical direction becomes longer. Thus, at late times the magnetic field and velocity are dominated by larger structures. The final state shown by the last panel of Figure 4 is quite similar to the ideal MHD case (Hawley & Balbus 1992). The magnetic field lines are almost horizontal, and two radial streams, one inward and the other outward,

TABLE 2
UNIFORM B_z SIMULATIONS

Model	Size	Grid	β_0	${\rm Re}_{M0}$	X_0	$\lambda_{\rm crit}/H$	$\sigma_{\rm max}/\Omega$	Orbits
Z1	$H \times H$	128×128	3200	100	2	0.11	0.75	4.5
Z2	$H \times H$	128×128	3200	100	0	0.064	0.74	5.9
Z3	$H \times H$	128×128	3200	100	-2	0.0	0.70	50
Z4	$H \times H$	128×128	3200	100	-5	...	...	50
Z5	$H \times H$	128×128	3200	10	2	0.11	0.72	5.0
Z6	$H \times H$	128×128	3200	10	0	0.064	0.70	5.4
Z7	$H \times H$	128×128	3200	10	-2	0.0	0.60	50
Z8	$H \times H$	128×128	3200	10	-5	...	...	50
Z9	$H \times H$	128×128	3200	1	2	0.12	0.51	6.4
Z10	$H \times H$	128×128	3200	1	0	0.091	0.43	9.7
Z11	$H \times H$	128×128	3200	1	-2	0.064	0.28	50
Z12	$H \times H$	128×128	3200	1	-5	...	...	50
Z13	$2H \times 2H$	128×128	3200	0.1	2	0.54	0.11	100
Z14	$2H \times 2H$	128×128	3200	0.1	0	0.64	0.074	100
Z15	$2H \times 2H$	128×128	3200	0.1	-2	0.91	0.037	100
Z16	$2H \times 2H$	128×128	3200	0.1	-5	...	...	100

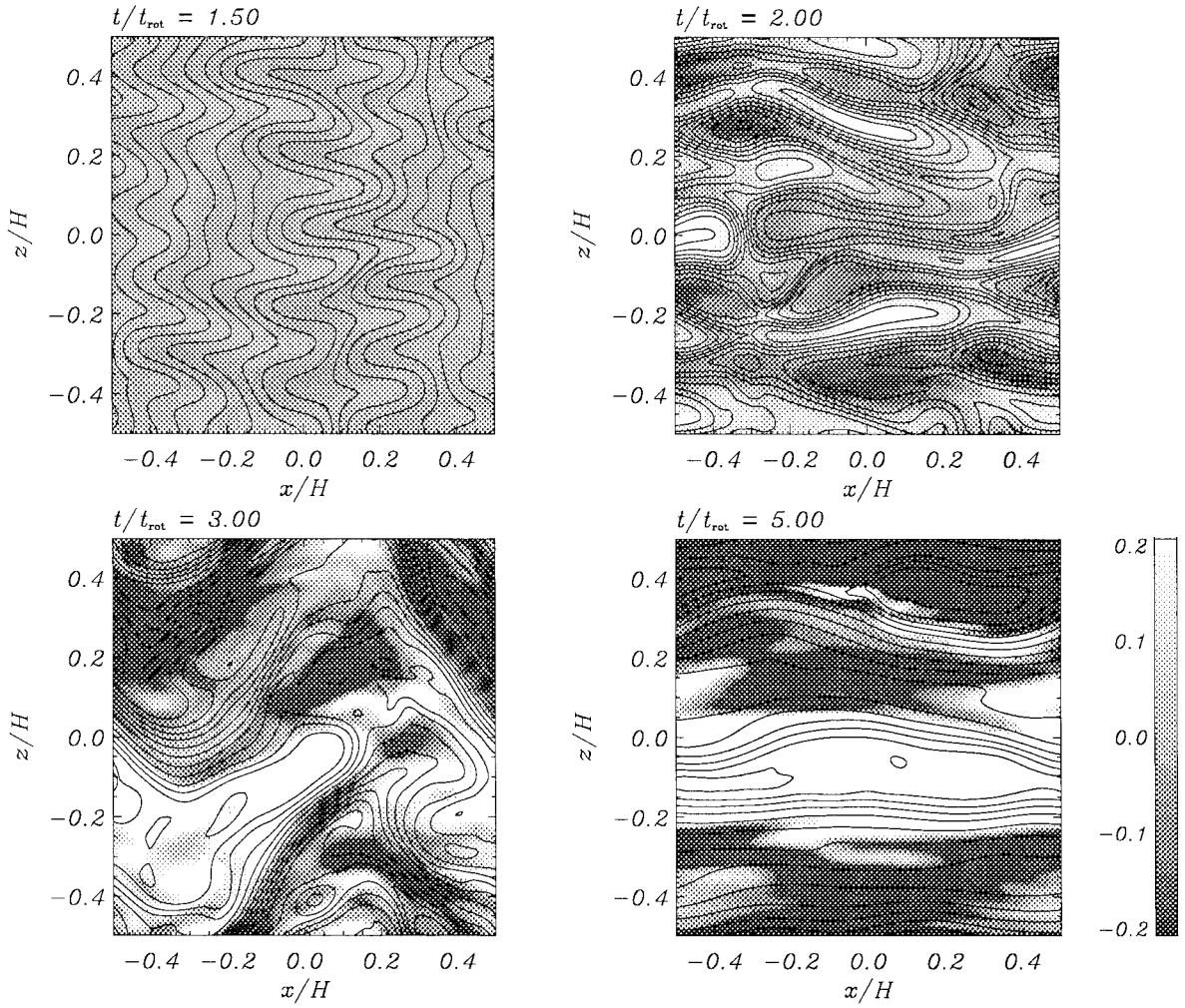

FIG. 4.—Magnetic field lines (*solid*) and radial velocity, $\delta v_x/c_{s0}$ (*gray color*) in model Z5 ($\beta_0 = 3200$, $\mathrm{Re}_{M0} = 10$, and $X_0 = 2$) at orbits 1.5, 2, 3, and 5

occupy the computational box. The increase of the magnetic energy continues without saturation until it exceeds $10P_0$ and the calculation is stopped.

Figure 5 shows the time evolution of the volume-averaged magnetic energy $\langle B^2/8\pi\rangle$ for models with $X_0 = 2$, 0, and -2 (model Z5, Z6, and Z7). The magnetic Reynolds number of these models is $\mathrm{Re}_{M0} = 10$. As mentioned above, the $X_0 = 2$ and 0 runs show unbounded exponential growth. Interestingly, the $X_0 = -2$ run shows amplification of the magnetic energy by an order of magnitude during the linear phase, followed by saturation at finite amplitude. This amplitude is sustained for at least 50 orbits.

We find that the growth of the MRI saturates for all models with $X_0 < 0$. Figure 6 shows images of typical time evolution of the field lines in a saturated model (Z7). The angular momentum perturbations $\delta v_y = v_y - v_{y0}$ are also shown by gray color contours. Obviously, smaller scale fluctuations are amplified in the linear phase compared to the model with $X_0 = 2$ (shown in Fig. 4). Larger scale structures do not dominate at the nonlinear stage for $X_0 < 0$, because small-wavelength perturbations are always unstable even after the field is amplified by the MRI (see § 5.1).

The nonlinear stage of model Z7 is MHD turbulence as shown by the last panel of Figure 6. The efficiency of angular momentum transport is measured by the turbulent stress w_{xy}, which is the sum of the Maxwell stress, $-B_xB_y/4\pi$, and

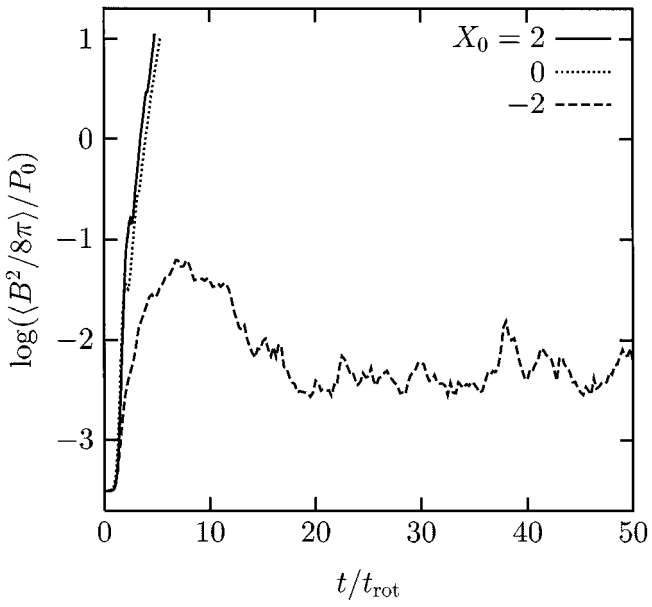

FIG. 5.—Time evolution of the volume-averaged magnetic energy $\langle B^2/8\pi\rangle/P_0$ for model Z5 ($X_0 = 2$), Z6 ($X_0 = 0$), and Z7 ($X_0 = -2$). The plasma beta and the magnetic Reynolds number of these models are $\beta_0 = 3200$ and $\mathrm{Re}_{M0} = 10$.

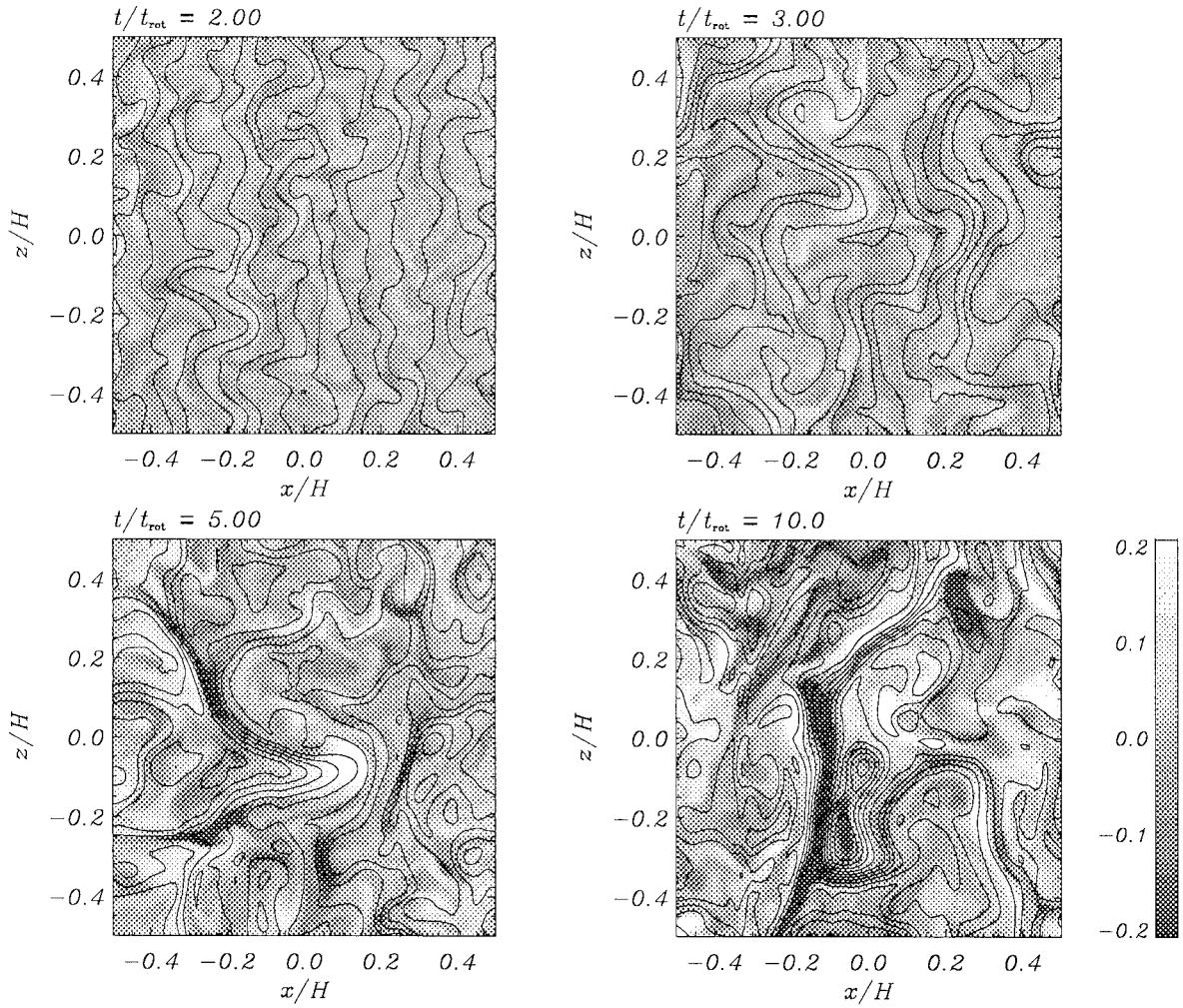

FIG. 6.—Magnetic field lines (*solid*) and angular momentum perturbation, $\delta v_y/c_{s0}$ (*gray color*) in model Z5 ($\beta_0 = 3200$, $\mathrm{Re}_{M0} = 10$, and $X_0 = -2$) at orbits 2, 3, 5, and 10.

the Reynolds stress, $\rho v_x \delta v_y$. The α parameter of Shakura & Sunyaev (1973) can then be expressed as $\alpha = w_{xy}/P_0$. The Maxwell stress is well-correlated with the magnetic energy, so that the time evolution of the stress is similar to that of the magnetic energy shown by Figure 5. We find that the saturation level of the Maxwell and Reynolds stresses are almost the same in model Z7. The time- and volume-averaged stresses are $\langle\langle -B_x B_y/4\pi\rangle\rangle/P_0 = 1.4 \times 10^{-3}$ and $\langle\langle \rho v_x \delta v_y\rangle\rangle/P_0 = 1.3 \times 10^{-3}$. The turbulence in this case is slightly anisotropic: the components of the magnetic and perturbed kinetic energy are $\langle\langle B_y^2\rangle\rangle = 4.6\langle\langle B_x^2\rangle\rangle = 1.8\langle\langle B_z^2\rangle\rangle$ and $\langle\langle \rho \delta v_y^2\rangle\rangle = 1.2\langle\langle \rho v_x^2\rangle\rangle = 1.4\langle\langle \rho v_z^2\rangle\rangle$.

The effective Hall parameter in the nonlinear regime is defined as

$$X_{\mathrm{eff}} \equiv \frac{cB_z\Omega}{2\pi e n_e v_{\mathrm{A}}^2} = \frac{2c\rho B_z \Omega}{e n_e B^2} . \tag{30}$$

Because the Hall parameter is inversely proportional to the field strength, the volume-averaged value $|\langle X_{\mathrm{eff}}\rangle|$ decreases as the field is amplified. The time-averaged value is $\langle\langle X_{\mathrm{eff}}\rangle\rangle = -0.16$ for model Z7, which started with $X_0 = -2$. At the end of model Z5, the volume-averaged effective Hall parameter is $\langle X_{\mathrm{eff}}\rangle \sim 10^{-4}$. The sign of $\langle X_{\mathrm{eff}}\rangle$ remains unchanged for both models. Thus, the importance of the Hall term becomes smaller as the MRI amplifies the field strength in the disk. When the field is amplified, the magnetic Reynolds number at the nonlinear stage $\langle v_{\mathrm{A}z}^2/\eta\Omega\rangle$ increases, and then ohmic dissipation also becomes less effective (Sano et al. 1998).

When $\mathrm{Re}_{M0} < 1$, the growth of the MRI saturates even without the Hall term (Sano et al. 1998). Thus, we find the Hall term has less effect in this case: the nonlinear evolution with $X_0 = \pm 2$ is quite similar to that of $X_0 = 0$. Ohmic dissipation controls the MRI in these cases, and the dependence on X_0 is very small except for the linear growth rate. Figure 7 shows the time evolution of the azimuthal component of the magnetic energy $\langle B_y^2/8\pi\rangle$ for the models with $\mathrm{Re}_{M0} = 0.1$ and $X_0 = 2$, 0, and -2 (model Z13, Z14, and Z15). The linear growth phase continues until a few tens of orbits because of the small growth rates in these models. The magnetic energy is amplified up to the initial thermal energy $\sim P_0$ for all the models. However, the energy is not sustained and finally dies out after 100 orbits. The Maxwell stress at the end of the calculation is very small for these cases, $\langle\langle -B_x B_y/4\pi\rangle\rangle/P_0 \sim 10^{-9}$.

Although the magnetic field returns to its initial configuration after 100 orbits, we do not see the MRI reemerge. In three dimensions, reemergence of the MRI on the background field (which can never be dissipated) leads to strong

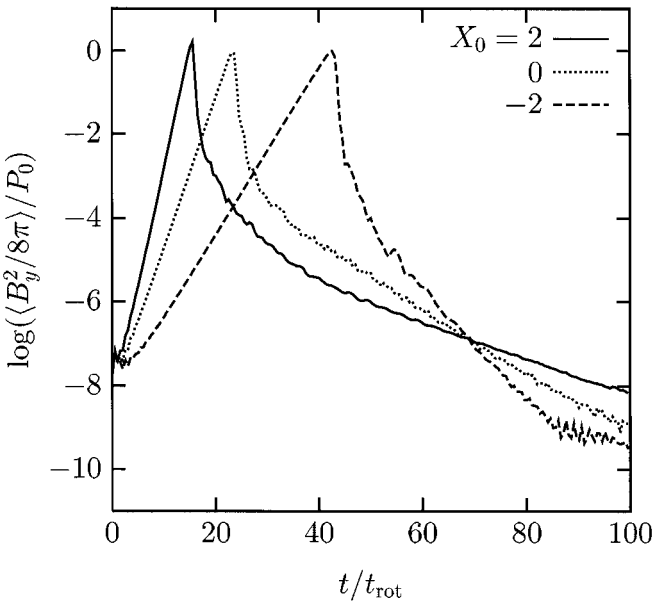

FIG. 7.—Time evolution of the azimuthal component of the magnetic energy $\langle B_y^2/8\pi\rangle/P_0$ for model Z13 ($X_0 = 2$), Z14 ($X_0 = 0$), and Z15 ($X_0 = -2$). The plasma beta and the magnetic Reynolds number of these models are $\beta_0 = 3200$ and $\mathrm{Re}_{M0} = 0.1$.

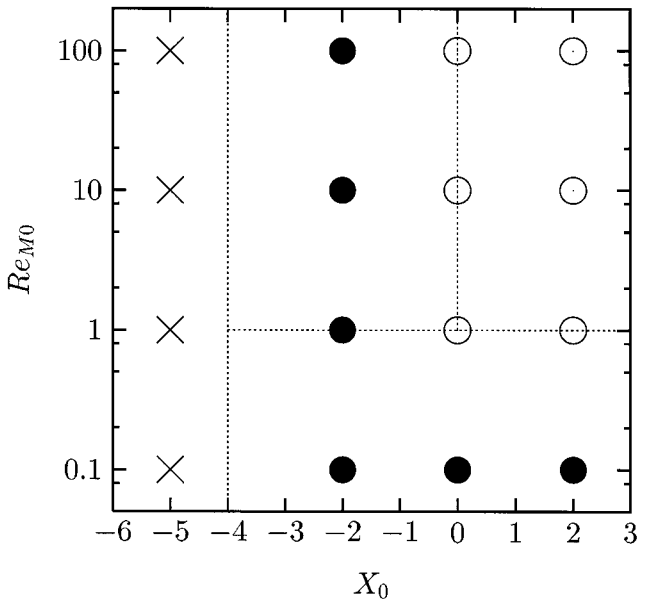

FIG. 8.—Final state for calculated disk models with a uniform vertical field. Filled circles denote models in which the growth of the MRI saturates as MHD turbulence in the nonlinear stage. Open circles denote models which evolve into a channel flow that grows without bound. Crosses denote models which are linearly stable to the MRI. The parameter space (X_0, Re_{M0}) is divided into four regions shown by the dotted lines according to the characteristic of the linear dispersion relation (see § 5.1).

fluctuations in, e.g., the Maxwell stress (Fleming et al. 2000). In these two-dimensional simulations, the magnetic and perturbed kinetic energy is nearly comparable at the end of the linear growth phase, so that the kinetic energy is $\langle \rho \delta v^2/2\rangle \sim 0.2 P_0 \gg B_0^2/8\pi$. After that, the magnetic energy starts decaying while the kinetic energy remains larger than its initial value. The kinetic energy is contained mostly in velocity along the field (vertical) direction. This flow is subthermal but super Alfvénic; this may suppress further growth of the MRI.

The evolution of the MRI on uniform vertical fields in two dimensions is summarized by Figure 8. The character of the nonlinear regime in the two-dimensional parameter space defined by Re_{M0} and X_0 is denoted by open circles for simulations that result in unbounded growth of the channel solution, filled circles for simulations that result in saturation and eventual decay, and crosses for simulations that show no growth at all. We find that when $\mathrm{Re}_{M0} \gtrsim 1$ and $X_0 \geq 0$, an unbounded two-channel flow emerges in the nonlinear regime. Saturation at finite amplitude occurs when $X_0 < 0$ or $\mathrm{Re}_{M0} \lesssim 1$. Finally, if $X_0 < -4$, all modes are stable: no linear growth can be seen for the models with $X_0 = -5$ (model Z4, Z8, Z12, and Z16) shown by crosses in the figure.

4.2. *Two-dimensional Simulations with Zero-Net Flux Vertical Fields*

Next we consider models with a zero-net flux vertical field, $B_z(x) = B_0 \sin(2\pi x/L_x)$. In the ideal MHD case with this initial field, the MRI evolves into a transient phase of MHD turbulence that eventually dies away (Hawley & Balbus 1992). For this initial field, the Hall parameter is given by $X(x) = X_0/\sin(2\pi x/L_x)$, where $X_0 = 2c\rho_0\Omega/en_{e0}B_0$. Thus, the region $x < 0$ has positive X, while the region $x > 0$ has negative X, and the minimum of $|X(x)|$ is X_0. Table 3 lists the models computed with a zero-net flux. The initial plasma beta β_0, the critical wavelength $\lambda_{\rm crit}$, and the

TABLE 3
ZERO-NET FLUX B_z SIMULATIONS

Model	Size	Grid	β_0	Re_{M0}	X_0	$\lambda_{\rm crit}/H$	$\sigma_{\rm max}/\Omega$	Orbits
S1.....	$H \times H$	128×128	3200	100	0	0.064	0.74	100
S2.....	$H \times H$	128×128	3200	100	2	0.11	0.75	100
S3.....	$H \times H$	128×128	3200	10	0	0.064	0.70	100
S4.....	$H \times H$	128×128	3200	10	2	0.11	0.72	100
S5.....	$H \times H$	128×128	3200	1	0	0.091	0.43	100
S6.....	$H \times H$	128×128	3200	1	2	0.12	0.51	100
S7.....	$H \times H$	128×128	3200	1	10	0.22	0.64	100
S8.....	$H \times H$	128×128	3200	1	100	0.65	0.74	10
S9.....	$H \times H$	128×128	3200	0.1	0	0.64	0.074	50
S10.....	$H \times H$	128×128	3200	0.1	10	0.40	0.23	50
S11.....	$H \times H$	128×128	3200	0.1	100	0.66	0.62	50
S12.....	$H \times H$	128×128	3200	0.1	1000	2.0	0.74	50

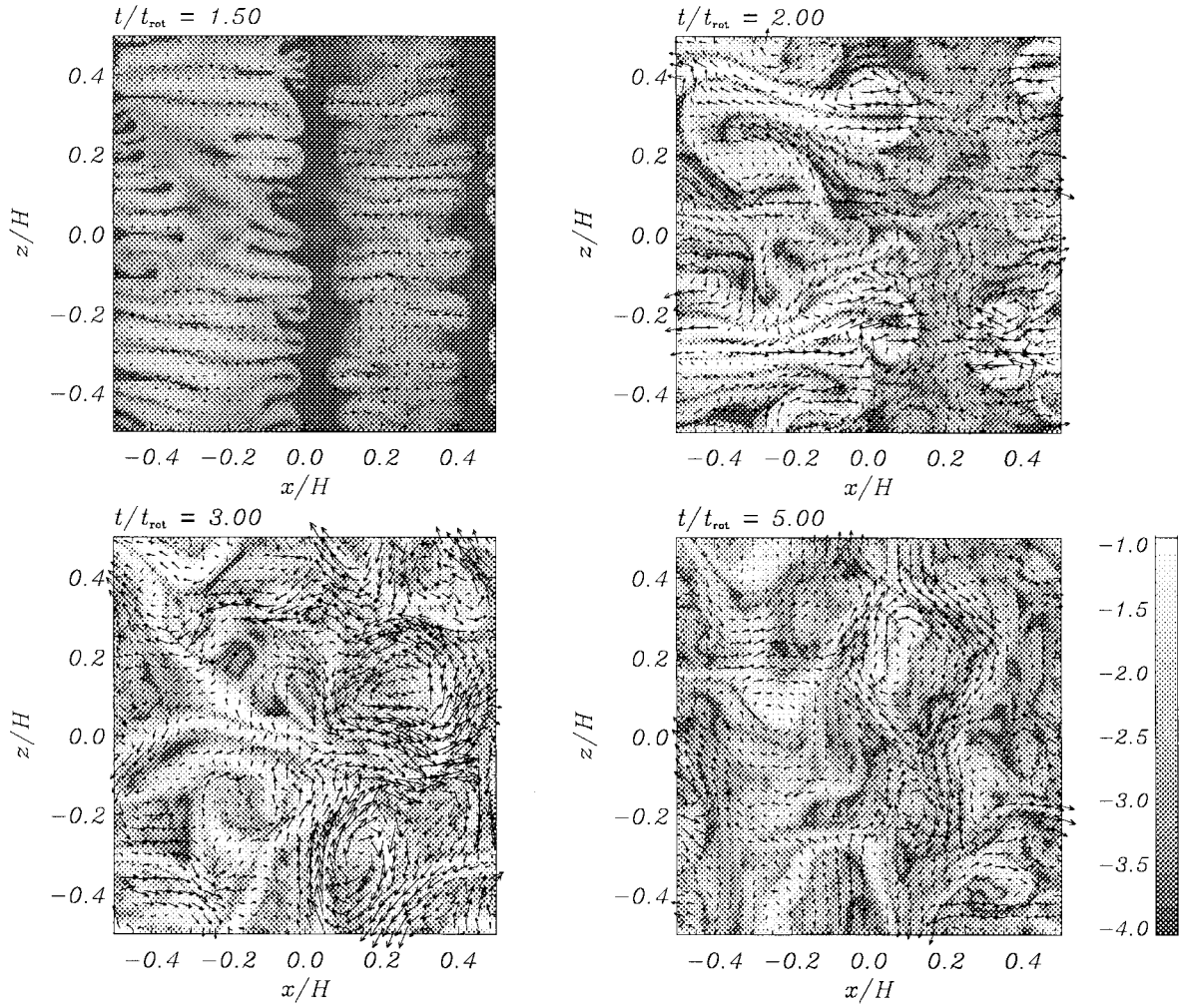

FIG. 9.—Magnetic field energy, $\log(B^2/8\pi P_0)$ (*gray color*), and velocity field (*arrows*) in model S2 ($\beta_0 = 3200$, $\mathrm{Re}_{M0} = 100$, and $X_0 = 2$) at orbits 1.5, 2, 3, and 5.

maximum growth rate $\sigma_{\max}$ are given for $B_z = B_0$ and $X = X_0$.

Figure 9 shows images of the magnetic energy in model S2, with $\mathrm{Re}_{M0} = 100$ and $X_0 = 2$. The velocity field is also shown by arrows. Most of the region with negative X is stable because the Hall parameter $X < -4$. The growth of the MRI is seen mainly in the region with positive X, as evident in the first panel of Figure 9. The growth in $x < 0$ gradually affects the structure of the region $x > 0$. The amplified magnetic field spreads across the entire computational domain by 3 orbits, after that the amplified magnetic energy is sustained for at least 100 orbits.

Figure 10 shows the time evolution of the magnetic energy for $\mathrm{Re}_{M0} = 100$, 10, and 1 with and without the Hall term ($X_0 = 0$ and 2). For the $\mathrm{Re}_{M0} = 100$ and 10 runs, the magnetic energy is sustained until 100 orbits. In the turbulent state the magnetic and the perturbed kinetic energy are equipartitioned. Since the vertical component of the magnetic energy, which is the seed of the MRI, continues decaying throughout the evolution, the activity of the turbulence gradually weakens over time in both runs. Therefore, active MHD turbulence is a transient phenomenon in these cases. When $\mathrm{Re}_{M0} = 100$, the Maxwell stress at the end of the calculation is $\langle\langle -B_x B_y/4\pi\rangle\rangle/P_0 = 1.6 \times 10^{-5}$ and 2.4×10^{-8} in the $X_0 = 0$ and 2 run, respectively. Only the toroidal field remains at late phases of the evolution. In two dimensions, a

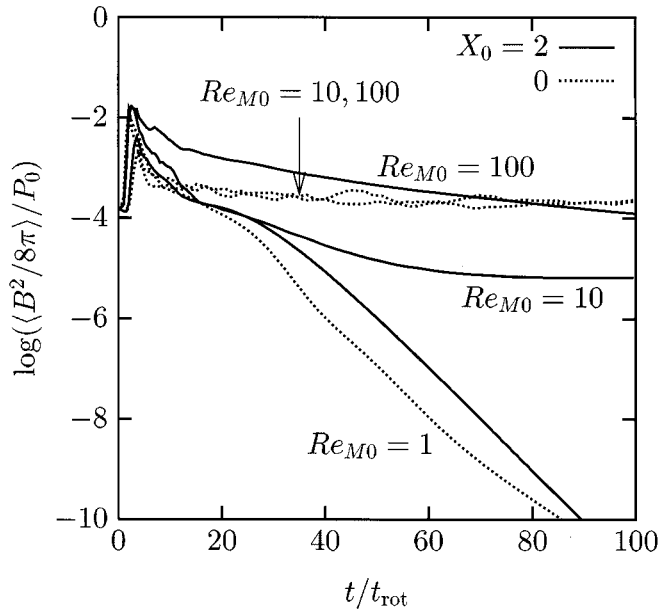

FIG. 10.—Time evolution of the magnetic energy $\langle\langle B^2/8\pi\rangle\rangle/P_0$ for model S1 ($\mathrm{Re}_{M0} = 100$ and $X_0 = 0$), S2 ($\mathrm{Re}_{M0} = 100$ and $X_0 = 2$), S3 ($\mathrm{Re}_{M0} = 10$ and $X_0 = 0$), S4 ($\mathrm{Re}_{M0} = 10$ and $X_0 = 2$), S5 ($\mathrm{Re}_{M0} = 1$ and $X_0 = 0$), and S6 ($\mathrm{Re}_{M0} = 1$ and $X_0 = 2$). The plasma beta of these models is $\beta_0 = 3200$.

disk with a purely toroidal field is stable to the MRI. However, nonaxisymmetric unstable modes could grow from the toroidal field and sustain MHD turbulence in three dimensions.

The evolution of more resistive models with $\mathrm{Re}_{M0} = 1$ and $X_0 = 0$ and 2 is quite different. The magnetic energy is amplified for several orbits, but then dies out. The decay time of the magnetic energy is about 5 orbits. The diffusion time $t_{\rm diff}$ of magnetic fields for a length scale l is given by

$$\frac{t_{\rm diff}}{t_{\rm rot}} = \frac{l^2}{\eta t_{\rm rot}} = 5.1 \times 10^2 \mathrm{Re}_{M0} \left(\frac{\beta_0}{3200}\right) \left(\frac{l}{H}\right)^2 . \quad (31)$$

Thus, the decay time corresponds to the diffusion time $t_{\rm diff}$ with $l \sim 0.1H \sim \lambda_{\rm crit}$.

The Hall parameter can take values up to about $100/\mathrm{Re}_{M0}$ (see eq. [16]) when the disk is in the Hall regime. Thus, a small magnetic Reynolds number Re_{M0} may give a very large Hall parameter X_0. Since the growth rate of the MRI is enhanced by large X_0 at small Re_{M0}, it is important to examine whether significant growth can occur in models with very large X_0. Models S7 and S8 have $\mathrm{Re}_{M0} = 1$, and $X_0 = 10$ and 100, respectively. The evolution of the $X_0 = 10$ run shows decay of the magnetic energy similar to the $X_0 = 2$ run (model S6). On the other hand, for $X_0 = 100$, active turbulence is initiated and sustained for at least 10 orbits. Figure 11 shows the time evolution of each component of the magnetic field in this run. As in the other active turbulent models, the Maxwell stress is strongly correlated with the magnetic energy and the time evolution of the stress is resemble to that of the magnetic energy. The stress is amplified up to $10^{-3}P_0$ and sustained until 10 orbits. This saturation level is comparable to or slightly larger than those in the less resistive models ($\mathrm{Re}_{M0} = 100$, 10) at the same phase.

For more resistive models with $\mathrm{Re}_{M0} = 0.1$, the nonlinear evolution in all cases (models S9–S12) shows rapid decay of the magnetic field even with very large X_0. The decay timescale of the magnetic energy is very short, about an orbit. In the $X_0 = 1000$ run with $\mathrm{Re}_{M0} = 0.1$ (model S12), the critical wavelength of the MRI is longer than the scale height of the disk H, or the vertical box size. No linear growth of the MRI can be seen in the calculation, nor would the MRI be present for these parameters in actual disks.

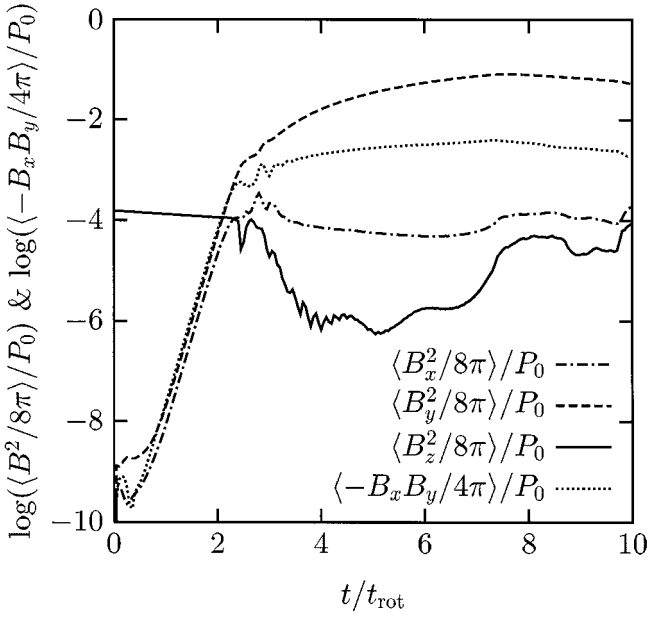

FIG. 11.—Time evolution of each component of the magnetic energy and the Maxwell stress in model S8 ($\beta_0 = 3200$, $\mathrm{Re}_{M0} = 1$, and $X_0 = 100$).

5. DISCUSSION

5.1. *Interpretation of the Two-dimensional Evolution*

The axisymmetric MRI evolves into a channel flow or MHD turbulence, depending on the parameters Re_{M0} and X_0 (provided linearly unstable modes exist at all). The results summarized in Figure 8 reflect the linear properties of the MRI. From the dispersion relation, the parameter space $X_0 > -4$ can be divided into three regions, as shown by dotted lines in Figure 8. When $\mathrm{Re}_{M0} \gtrsim 1$ and $X_0 \geq 0$, the characteristic wavelength of the MRI is proportional to v_A/Ω, and a critical wavelength exists. For this case, the evolution of the MRI shows an inverse cascade of the magnetic energy, and a two-channel flow emerges without saturation. This is because the characteristic scale increases as the field strength is amplified by the growth of the MRI. In the second region ($\mathrm{Re}_{M0} \lesssim 1$), the dispersion relation has a critical wavelength, but the most unstable wavelength is proportional to $\eta/v_{\rm A}$, that is inversely proportional to the field strength. In the third region ($X_0 < 0$), there is no characteristic scale of the MRI. Then smaller scale fluctuations are always unstable. Therefore, models in these last two regions show no evidence for an inverse cascade; instead they evolve into MHD turbulence.

Models with $\beta = 800$ also show the same characteristics as the models plotted in Figure 8, implying these results are independent of the initial field strength. Estimation of the saturated amplitude of the Maxwell stress, which determines the efficiency of angular momentum transport in actual accretion disks, requires three-dimensional simulations of the MRI. In three-dimensional simulations that include only the ohmic dissipation, the saturation amplitude of the Maxwell stress is larger if the MRI has an inverse cascade (Sano & Inutsuka 2001). Local three-dimensional simulations of the MRI in Hall MHD are presented in Sano & Stone (2002).

5.2. *Definition of Magnetic Reynolds Number*

In this paper we have defined the magnetic Reynolds number as $\mathrm{Re}_M = v_{\rm A}^2/\eta\Omega$, and used Re_{M0} to denote the value of this number in the initial state. Both a linear analysis of the MRI including ohmic dissipation, as well as local three-dimensional simulations with an initial uniform vertical field reveal that the critical number required to generate significant MHD turbulence and angular momentum transport is $\mathrm{Re}_{M0} \sim 1$ (Sano & Inutsuka 2001). If $\mathrm{Re}_{M0} > 1$ the evolution and saturated state of the MRI is little changed from the ideal MHD case, whereas if $\mathrm{Re}_{M0} < 1$ the growth rates and amplitude of the saturated state are both significantly reduced compared to the ideal MHD case.

In actual accretion disks, there is a minimum value for Re_M that results from the requirement that the critical wavelength of unstable modes in the very resistive regime $\lambda_{\rm MRI} \sim \eta/v_{\rm A}$ be less than the disk thickness H (Sano & Miyama 1999). This requires $\mathrm{Re}_{M0} > v_{\rm A}/c_s$, which can also be used as a stability criterion (Gammie 1996; Igea & Glassgold 1999; Sano et al. 2000). If the field strength of accretion

disks is subthermal and $v_A/c_s < \mathrm{Re}_{M0} < 1$, the MRI will be present, but the growth rate, saturated amplitude, and angular momentum transport rate will all be reduced compared to the ideal MHD case. In practice, the largest value for the ratio v_A/c_s that can be reached in an accretion disk is probably unity (otherwise the field will escape the disk via buoyancy). In this case, the magnetic Reynolds number becomes $\mathrm{Re}'_M = c_s^2/\eta\Omega$ (Gammie & Menou 1998; Fleming et al. 2000), with the critical value measured from three-dimensional simulations about 10^4. This last form is independent of the magnetic field strength in the disk, and therefore can be measured more easily with observations. However, even if the observed Re'_M is below the critical value 10^4, the MRI may still operate if $0.01 \lesssim v_A/c_s < 1$.

6. SUMMARY

We have shown that in both dwarf nova disks in quiescence, and in protoplanetary disks around young stars, the Hall term can be important to the linear properties of the MRI, and therefore must be included in realistic models of these systems. Next, we investigated the nonlinear evolution of the MRI in Hall MHD using axisymmetric two-dimensional simulations. Although three-dimensional simulations are essential for evaluating the efficiency of angular momentum transport in accretion disks, understanding the two-dimensional evolution will be very helpful to the interpretation of three-dimensional results. Fully three-dimensional simulations of the nonlinear regime of the MRI in Hall MHD are presented in a companion paper (Sano & Stone 2002).

Our findings are summarized as follows.

1. For dwarf nova disks in quiescence, both the Hall effect and ohmic dissipation are very important when the temperature is less than about 1500 K. The importance of these effects is very sensitive to the temperature of the disk.

2. In the region $r \lesssim r_H$ in protoplanetary disks, the Hall term dominates over ohmic dissipation and ambipolar diffusion, assuming dust grains have settled out to the midplane. The critical radius $r_H \sim 10$–100 AU, and it depends mainly on the magnetic field strength in the disk. Inside a radius of $r_O \sim 1$–5 AU, ohmic dissipation suppresses all modes of the MRI, except within about 0.1 AU where thermal ionization becomes important. If dust grains with the same size distribution as interstellar grains are well mixed throughout the disk (i.e., they have not settled to the midplane), r_O increases dramatically, and the entire disk is dominated by ohmic dissipation.

3. For models with an initially uniform B_z, the MRI evolves into either a two-channel flow which grows without bound (for $\mathrm{Re}_{M0} \gtrsim 1$ *and* $X_0 \geq 0$), or saturates as MHD turbulence (for $\mathrm{Re}_{M0} \lesssim 1$ *or* $X_0 < 0$). If $\mathrm{Re}_{M0} \lesssim 1$, saturation of the MRI occurs, but the amplified magnetic field eventually dies out.

4. For models with an initial zero-net flux vertical field, the MRI saturates as MHD turbulence, which either is sustained or eventually dies away depending on Re_{M0}. In this case, the evolution is determined mostly by the effect of ohmic dissipation and has little dependence on the Hall parameter X_0.

We thank Steven Balbus, Caroline Terquem, and Neal Turner for helpful discussions. Computations were carried out on VPP5000 at the National Astronomical Observatory of Japan and VPP700 at the Subaru Telescope, NAOJ.

APPENDIX

ALGORITHM FOR THE CALCULATION OF THE HALL TERM

We adopt an operator split solution procedure for the update of the magnetic field. Following the constraint transport method (Evans & Hawley 1988), the Hall electromotive force (EMF) $\mathscr{E}_H$ is calculated at the zone boundaries. For simplicity the one-dimensional algorithm (in the x direction) is described here; the extension to multiple dimensions is straightforward. In the one-dimensional case, the tangential components of the magnetic field and EMF are defined at the zone center and zone boundary, respectively, and the x component of the magnetic field is constant B_x.

The change of the magnetic field due to the Hall EMF is given by

$$\frac{\partial \boldsymbol{B}}{\partial t} = \nabla \times \mathscr{E}_H = \nabla \times [-Q_H(\nabla \times \boldsymbol{B}) \times \boldsymbol{B}] , \tag{A1}$$

where $Q_H = c/4\pi e n_e$ is assumed to be constant. Each component of the induction equation (A1) is written as

$$\frac{\partial B_y}{\partial t} = -\frac{\partial \mathscr{E}_{Hz}}{\partial x} = Q_H B_x \frac{\partial^2 B_z}{\partial x^2} , \tag{A2}$$

$$\frac{\partial B_z}{\partial t} = \frac{\partial \mathscr{E}_{Hy}}{\partial x} = -Q_H B_x \frac{\partial^2 B_y}{\partial x^2} , \tag{A3}$$

where

$$\mathscr{E}_{Hy} = -Q_H B_x \frac{\partial B_y}{\partial x} , \tag{A4}$$

$$\mathscr{E}_{Hz} = -Q_H B_x \frac{\partial B_z}{\partial x} . \tag{A5}$$

For the update from t^n to t^{n+1}, the partially time-advanced values of the Hall EMF $\mathscr{E}_H^{n+1/2}$ at $t^{n+1/2}$ are needed. From equations (A4) and (A5), the time-advanced Hall EMF at a zone $x = i$ and $t^{n+1/2}$ is given by

$$\mathscr{E}_{Hy,i}^{n+1/2} = -Q_H B_x \frac{B_{y,i}^{n+1/2} - B_{y,i-1}^{n+1/2}}{\Delta x} , \tag{A6}$$

$$\mathscr{E}_{Hz,i}^{n+1/2} = -Q_H B_x \frac{B_{z,i}^{n+1/2} - B_{z,i-1}^{n+1/2}}{\Delta x} , \tag{A7}$$

where Δx is the grid scale. To evaluate $B^{n+1/2}$, we use equations (A2) and (A3); the induction equation including only the Hall EMF. Then the partial update of B_y and B_z is given by

$$B_{y,i}^{n+1/2} = B_{y,i}^n + \frac{\Delta t}{2} Q_H B_x \frac{B_{z,i+1}^n - 2B_{z,i}^n + B_{z,i-1}^n}{(\Delta x)^2} , \tag{A8}$$

$$B_{z,i}^{n+1/2} = B_{z,i}^n - \frac{\Delta t}{2} Q_H B_x \frac{B_{y,i+1}^n - 2B_{y,i}^n + B_{y,i-1}^n}{(\Delta x)^2} , \tag{A9}$$

where Δt is the time step.

Since our update of the Hall term is time explicit, we also must add a new time step constraint. The frequency of the whistler wave is approximately given by $\omega \approx Q_H B_x k^2$, where k is the wavenumber, thus the group velocity is $2Q_H B_x k$. The new constraint on the time step is then

$$\Delta t \le \frac{\Delta x}{2Q_H B_x k} \equiv \frac{(\Delta x)^2}{4\pi Q_H B_x} , \tag{A10}$$

where we assume $k = 2\pi/\Delta x$.

In addition to checking the numerical growth rates of the MRI in Hall MHD with the predictions of linear theory (Fig. 3), we have also tested our algorithm by comparing the numerically measured phase velocity of whistler waves with the linear dispersion relation. For this test, we adopt a uniform density ρ and a uniform magnetic field parallel to the x-axis, B_x ($B_y = B_z = 0$), and consider the propagation of linear waves proportional to $\exp i(kx - \omega t)$ in the incompressible limit. The dispersion equation without the Hall effect is $\omega^2 = v_A^2 k^2$, where $v_A^2 = B_x^2/4\pi\rho$. If the Hall term is included, the dispersion equation is then written as

$$(\omega^2 - v_A^2 k^2)^2 = Q_H^2 B_x^2 k^4 \omega^2 . \tag{A11}$$

Figure 12 shows the dispersion relation obtained from equation (A11). Due to the Hall effect, the Alfvén wave ($\omega/v_A k = 1$) splits into left- and right-circularly polarized waves. The right (whistler) wave can propagate much faster than the Alfvén wave. Numerically obtained phase velocities are also shown in the figure by open circles. Each mode is calculated using a one-dimensional simulation of the propagation of a linear wave with 32 grid zones per a wavelength. The numerically measured phased velocities agree with the dispersion relation very well (better than 1%). This shows that our algorithm accurately captures the characteristics of Hall MHD.

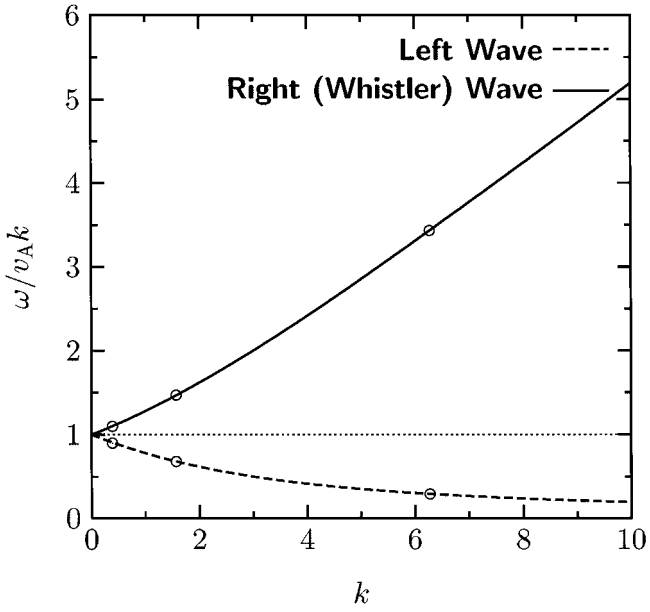

FIG. 12.—Dispersion relation of the left- and right-circularly polarized wave traveling along field lines. The Alfvén wave for the case without the Hall effect ($\omega/v_A k = 1$) is shown by dotted line for comparison. Open circles denote numerically measured phase velocity in one-dimensional simulations.

REFERENCES

Balbus, S. A., & Hawley, J. F. 1991, ApJ, 376, 214
Balbus, S. A., & Terquem, C. 2001, ApJ, 552, 235
Blaes, O. M., & Balbus, S. A. 1994, ApJ, 421, 163
Brandenburg, A., Nordlund, Å., Stein, R. F., & Torkelsson, U. 1995, ApJ, 446, 741
Cannizzo, J. K. 1993, ApJ, 419, 318
Cuzzi, J. N., Dobrovolskis, A. R., & Champney, J. M. 1993, Icarus, 106, 102
Draine, B. T., Roberge, W. G., & Dalgarno, A. 1983, ApJ, 264, 485
Evans, C. R., & Hawley, J. F. 1988, ApJ, 332, 659
Fleming, T. P., Stone, J. M., & Hawley, J. F. 2000, ApJ, 530, 464
Gammie, C. F. 1996, ApJ, 457, 355
Gammie, C. F., & Menou, K. 1998, ApJ, 492, L75
Hawley, J. F., & Balbus, S. A. 1992, ApJ, 400, 595
Hawley, J. F., Gammie, C. F., & Balbus, S. A. 1995, ApJ, 440, 742
Hawley, J. F., & Stone, J. M. 1998, ApJ, 501, 758
Hodgson, L. S., & Brandenburg, A. 1998, A&A, 330, 1169
Igea, J., & Glassgold, A. E. 1999, ApJ, 518, 848
Jin, L. 1996, ApJ, 457, 798
Mac Low, M.-M., Norman, M. L., Königl, A., & Wardle, M. 1995, ApJ, 442, 726
Mathis, J. S., Rumpl, W., & Nordsieck, K. H. 1977, ApJ, 217, 425
Millar, T. J., Farquhar, P. R. A., & Willacy, K. 1997, A&AS, 121, 139
Regős, E. 1997, MNRAS, 286, 97
Sano, T., & Inutsuka, S. 2001, ApJ, 561, L179
Sano, T., Inutsuka, S., & Miyama, S. M. 1998, ApJ, 506, L57
———. 1999, in Numerical Astrophysics, ed. S. M. Miyama, K. Tomisaka, & T. Hanawa (Dordrecht: Kluwer), 383
Sano, T., & Miyama, S. M. 1999, ApJ, 515, 776
Sano, T., Miyama, S. M., Umebayashi, T., & Nakano, T. 2000, ApJ, 543, 486
Sano. T., & Stone, J. M. 2002, ApJ, submitted
Shakura, N. I., & Sunyaev, R. A. 1973, A&A, 24, 337
Stone, J. M., Gammie, C. F., Balbus, S. A., & Hawley, J. F. 2000, in Protostars & Planets IV, ed. V. G. Mannings, A. P. Boss, & S. Russell (Tuscon: Univ. Arizona Press), 589
Stone, J. M., & Norman, M. L. 1992, ApJS, 80, 791
Umebayashi, T., & Nakano, T. 1981, PASJ, 33, 617
———. 1988, Prog. Theor. Phys. Suppl., 96, 151
van Leer, B. 1979, J. Comput. Phys., 32, 101
Wardle, M. 1999, MNRAS, 307, 849
Wardle, M., & Ng, C. 1999, MNRAS, 303, 239